Research Article | Vol. 30, No. 3 / 31 Jan 2022 / Optics Express 4058
Optics EXPRESS

# Absorption and scattering in perfect thermal radiation absorber-emitter metasurfaces

YOSHIAKI NISHIJIMA,[1,2,*] NAOKI TO,[1] ARMANDAS BALČYTIS,[1] AND SAULIUS JUODKAZIS[2,3,4]

[1]Department of Electrical and Computer Engineering, Graduate School of Engineering, Yokohama National University, 79-5 Tokiwadai, Hodogaya-ku, Yokohama 240-8501, Japan
[2]Institute of Advanced Sciences, Yokohama National University, 79-5 Tokiwadai, Hodogaya-ku, Yokohama 240-8501, Japan
[3]Optical Sciences Centre and ARC Training Centre in Surface Engineering for Advanced Materials (SEAM), School of Science, Swinburne University of Technology, Hawthorn VIC 3122, Australia
[4]Tokyo Tech World Research Hub Initiative (WRHI), School of Materials and Chemical Technology, Tokyo Institute of Technology, 2-12-1, Ookayama, Meguro-ku, Tokyo 152-8550, Japan
*nishijima-yoshiaki-sp@ynu.ac.jp

**Abstract:** Detailed spectral analysis of radiation absorption and scattering behaviors of metasurfaces was carried out via finite-difference time-domain (FDTD) photonic simulations. It revealed that, for typical metal-insulator-metal (MIM) nanodisc metasurfaces, absorbance and scattering cross-sections exhibit a ratio of $\sigma_{abs}/\sigma_{sca} = 1$ at the absorption peak spectral position. This relationship was likewise found to limit the attainable photo-thermal conversion efficiency in experimental and application contexts. By increasing the absorption due to optical materials, such as Cr metal nano-films typically used as an adhesion layer, it is possible to control the total absorption efficiency $\eta = \sigma_{abs}/\sigma_{sca}$ and to make it the dominant extinction mechanism. This guided the design of MIM metasurfaces tailored for near-perfect-absorption and emission of thermal radiation. We present the fabrication as well as the numerical and experimental spectral characterisation of such optical surfaces.



## 1. Introduction

Realization of perfect absorption is desirable in the field of photo-thermal, photo-voltaic energy conversion [1–5]. Especially radiation absorption in metal-insulator-metal (MIM) metasurfaces, which generally consist of a metal back-plate, dielectric layer, and a metal nano-structure, is currently applied for realizing a great variety of efficient photo-thermal energy converter designs [1,6–30]. Such converters also show significant promise in the mid-infrared (IR) wavelength range, where they are used as both IR radiation sources as well as detectors, notably for applications in optical sensing of volatile organic compounds (VOCs) [31–41]. Also, owing to their spectrally selective emissivity, metasurfaces can be harnessed as passive yet efficient radiative coolers at specific atmospheric IR transmission windows.

In most studies, the absorbance $A$ exhibited by a MIM metasurface is among its most important properties - implicitly treated as $A = I - R$, where $I$ is energy incident on the sample ($I = 1$ in the normalised presentation), whereas $R$ is the reflectance. This absorption relies on dissipation of optical energy in metals, although realization of perfect absorption is also considered using epsilon near zero (ENZ) materials [42–46] with permittivity $\varepsilon \equiv \tilde{n}^2 \rightarrow 0$. Similarly, coupling of ENZ and a meteasurfaces provides a viable path for attaining a highly absorbing layers [44]. For example, indium tin oxide (ITO) is a notable ENZ material candidate, however, its operation wavelength is highly dependent on specifically tailored optical constants. Therefore, precise control over dopant concentrations becomes an acute challenge in achieving a well-defined ENZ wavelength. In designing metasurfaces, nano-structures and functional layers are usually treated

#447885 https://doi.org/10.1364/OE.447885
Journal © 2022 Received 7 Nov 2021; revised 12 Jan 2022; accepted 15 Jan 2022; published 24 Jan 2022

Optics EXPRESS

rigorously, but the absorbance in the metal back plate of a MIM structure is scrutinised to a far lesser degree due to experimental difficulties in directly measuring the fraction of optical energy absorbed in it. The metal back plate is understood as a reflector with negligible transmittance owing to its considerable thickness. Hence, the scattered portion of radiation energy $S$ is either ignored or not explicitly accounted for, since it is assumed to be incorporated in $R$ or $T$ and is distributed among them.

As illustrated in Fig. 1, the relevant optical power balance equation is $I = A + R + T + S$ and $(I - R - T)$ corresponds to the extinction $Ext = A + S$, which accounts for all the energy removed from a propagating beam in a far-field measurement. In this representation $R$ corresponds to the specular and $S$ to the diffuse reflectance respectively. Due to a zero transmittance $T = 0$ of the MIM metasurface, both $R$ and $S$ manifest as a backward reflection of light. In the case of nanoparticles (nanodiscs in this work), their plasmonic resonance-related optical properties are derived from the Mie scattering by the structures. The the resonance bandwidth is defined by scattering rather than the inherently broadband absorption exhibited by electron plasmas in metals [47–53].

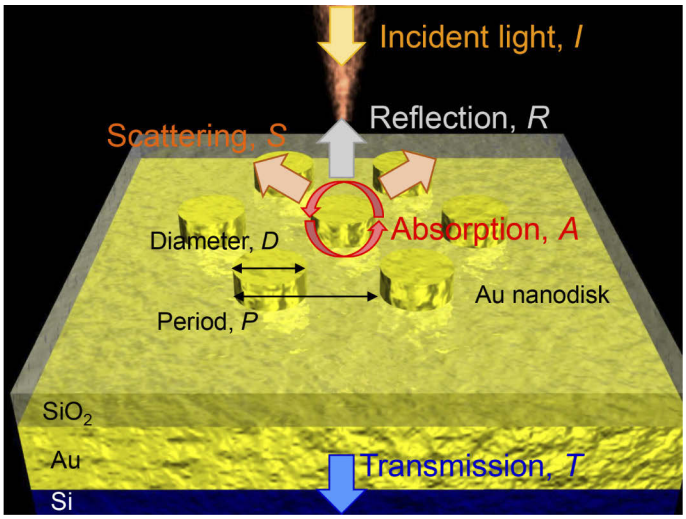


**Fig. 1.** Schematic illustration of the redistribution of incident optical energy $I$ once it impinges onto the MIM metasurface. When calculating absorbance $A$, scattered energy portion $S$ is usually incorporated into reflectance $R$ or transmittance $T$ so that their total amounts to unity $A + R + T = 1$.

Our previous reports on emissivity of metasurfaces with 10-nm-thin insulator layers confirmed that their thermal radiation spectral output qualitatively follows Kirchhoff's law [34]. However, it was noticed that thermal radiation emittance from metasurfaces was quantitatively lower than would be expected if Kirchhoff's law was rigorously obeyed, given the near-perfect anti-reflectance exhibited by the structure. This prompted the present study. MIM metasurfaces confine a significant portion of the resonant electro-magnetic field in the insulator layer, but a fraction of radiation energy is nevertheless localized around nanodsics and subject to scattering. Therefore, scattering effects are expected to notably effect metasurface optical response and its characterisation, and their control is vital to realization and demonstration perfect optical absorber performance. This issue was highlighted by Maccaferri *et. al* and a mitigation strategy by multi-layered metasurface design was proposed to spectrally separate the absorption and scattering effects [54].

Optics EXPRESS

The target of this study is a comparative analysis of absorption and its cross-section in fabricated MIM samples and FDTD simulations. It involved extensive metasurface parameter sweeps - including disk diameter $D$, period $P$, insulator thickness - and optimisation of the final design that was subsequently fabricated. Such analysis also revealed the effect of scattering on the thermal radiation emission behavior of such metasurfaces. According the Kirchhoff's law of thermal radiation, emittance is related to the absorbance $E = A$ but not to the scattered portion of energy $S$. Therefore, by increasing the absorption cross-section compared to the scattering one, the radiation emissivity would be also expected to increase. This conjecture is put to the test by way of numerical analysis and experimental verification, whereby we show interplay of the scattering and absorbance contributions in optical response of a MIM metasurface and the way to maximise absorbance towards a true perfect absorber with $A \rightarrow 1$ (or $A = I = 100\%$).

## 2. Experimental and modeling

### 2.1. FDTD simulations

FDTD simulations were performed using a commercially available solver software (ANSYS/Lumerical) on a homemade workstation with Dual CPU (AMD EPYC 7302 16 core $\times$ 2), 512 GB (32 GB $\times$ 16) of DDR4 memory. To simulate metasurface response in a broad wavelength range from visible to mid-infrared (MIR) wavelengths, material permittivity data for Au, Cr, Si and $SiO_2$ reported by Palik was employed [55–58]. In this study, reflectance spectra simulations were performed using a plane wave source set to illuminate the MIM structures from the top nanodisk-patterned side, incident along z-axis. The reflection readout monitor was placed above the light source. The MIM structure was framed along the x- and y-directions using periodic boundary conditions, whereas a perfectly matched layer (PML) was used for termination along the the z-coordinate axis. Absorption and scattering cross-section simulations were conducted on same configuration of MIM structures, key difference being that a total-field scattered-field (TFSF) light source was initialized. Two sets of power monitors were placed inside and outside of the TFSF source volume, respectively for calculating the absorbed and scattered optical powers.

### 2.2. Fabrication of metasurfaces

MIM structures were defined on a mirror-polished Si wafer substrate surface by first depositing a 5 nm Cr adhesion layer and 200 nm Au reflector metal films by thermal evaporation. Then, either 5 nm or 50 nm of Cr and 100, 150, 200 nm of $SiO_2$ were deposited using electron beam (EB)-evaporation. Electron beam lithography (EBL) was used to define periodic nanodisk patterns with individual feature diameters ranging form 600 nm to 4000 nm over $1 \times 1\text{mm}^2$ areas in a spin-coated ZEP520A positive tone resist. Pattern development was again followed by thermal evaporation deposition of 5 nm or 50 nm thickness Cr adhesion/absorber film, followed by 50 nm thickness of Au. Then, resist lift-off was performed using a heated organic solvent, N-Methyl-2-pyrolidone (NMP) at 100°C, until a metal layer deposited over the resist fully removed. Lastly, MIM metasurface samples were washed in acetone and methanol and blow-dried in air.

### 2.3. Optical measurements

Metasurface reflectance characterization was performed using a FTIR spectroscope system (FTIR-6600) with a microscopy attachment unit IRT-1000. Thermal radiation emission was likewise measured with the same FTIR-6600 and IRT-1000 setup by using the MIM metasurface as an external illumination source, connected to the spectroscope via a side port. The reference for reflection was a Au-mirror (98% reflectance at MIR wavelengths) and a paint with 94% emissivity was employed as a blackbody radiation standard. For best comparability the paint

Optics EXPRESS

was applied directly onto the MIM sample chips near the $1 \times 1$ mm$^2$ metasurface areas. Heating in thermal radiation output measurements was applied to the substrate by placing on a Peltier device and fixed with a thermal conductive grease. The devices were heated up to 150°C. Prior to measurement each sample was allowed to reach a steady thermal state over the course of at least a 30 minute a settling time.

## 3. Results and discussion

Figure 2 shows FDTD simulated extinction $Ext \equiv 1 - R$, as well as absorption, scattering and extinction cross-section (respectively $\sigma_{\text{abs}}$, $\sigma_{\text{sca}}$, $\sigma_{\text{ext}}$) spectra of MIM metasurfaces with fixed $D = 400$ nm disc diameter and $P = 800$ nm period values, but varying $SiO_2$ spacer thicknesses. For simple nanodisc metasurfaces, resonance wavelength of extinction 1-$R$ maximum matches that of the maximum $\sigma_{abs}$, $\sigma_{sca}$ and $\sigma_{ext}$. At this period-to-diameter ratio of $P/D = 2$ the interaction between adjacent nanodiscs (plasmonic gap mode) is negligible. Even if a collective grating effect is present, the optical properties of the metasurface are primarily defined by the interaction between dipole resonance of the individual nanodiscs and their induced mirror-charge oscillations in the metal ground plate [59]. Therefore, when the spacing between nanodisc and ground plate become smaller, the dipole-induced interaction is enhanced, causing a red-shift in the resonance wavelength. Both absorption and scattering are defined by the resonant interaction between a nanodisc and ground plate; $\sigma_{\text{sca}}$ increases for a thicker $SiO_2$ layer. This series of simulations revealed that both $\sigma_{\text{abs}}$ and $\sigma_{\text{sca}}$ are prominent at the minimum specular reflectance condition when overall extinction $Ext = 1 - R$ is at its maximum.

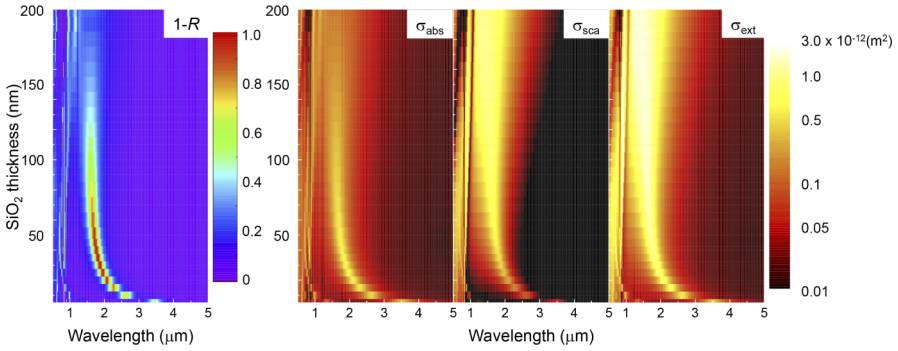


**Fig. 2.** FDTD simulated spectral variations of extinction $Ext = 1 - R$, and the respective cross-sections for absorption $\sigma_{\text{abs}}$, scattering $\sigma_{\text{sca}}$, and the total extinction $\sigma_{\text{ext}}$ with different $SiO_2$ insulator layer thickness.

This behavior is elaborated further in Fig. 3(a), which shows maximum $\sigma_{\text{abs}}$, $\sigma_{\text{sca}}$, $\sigma_{\text{ext}}$ at resonance wavelength plotted as a function of $SiO_2$ insulator thickness. The absorption cross-section $\sigma_{\text{abs}}$ rises until $t_d = 30$ nm, but starts to decrease when thicknesses of $SiO_2$ are increased further. At the same time, the scattering cross-section $\sigma_{\text{sca}}$ continues to increase up to a considerably higher $t_d = 150$ nm $SiO_2$ thickness. As shown in Fig. 3(b), at maximum extinction $Ext = 1 - R$, the absorption cross-section $\sigma_{\text{abs}}$ is likewise at its peak, yet the absorption/scattering cross section ratio $\eta = \sigma_{\text{abs}}/\sigma_{\text{sca}}$ at best becomes equal to 1.

The effect of MIM metasurface configuration on resonant mode localization is revealed by FDTD derived cross-sectional view plots in Fig. 3(c). It is evident that, until $SiO_2$ spacer thickness is at or below $t_d = 30$ nm, the majority of the optical field is tightly confined inside the insulator layer. However, as thicknesses become larger, the localization in the insulator layer is diminished, and modes start to exhibit a more pronounced dipolar character, typical for isolated nanodisk plasmonic structures. A majority of the optical field portion localized in the

Optics EXPRESS

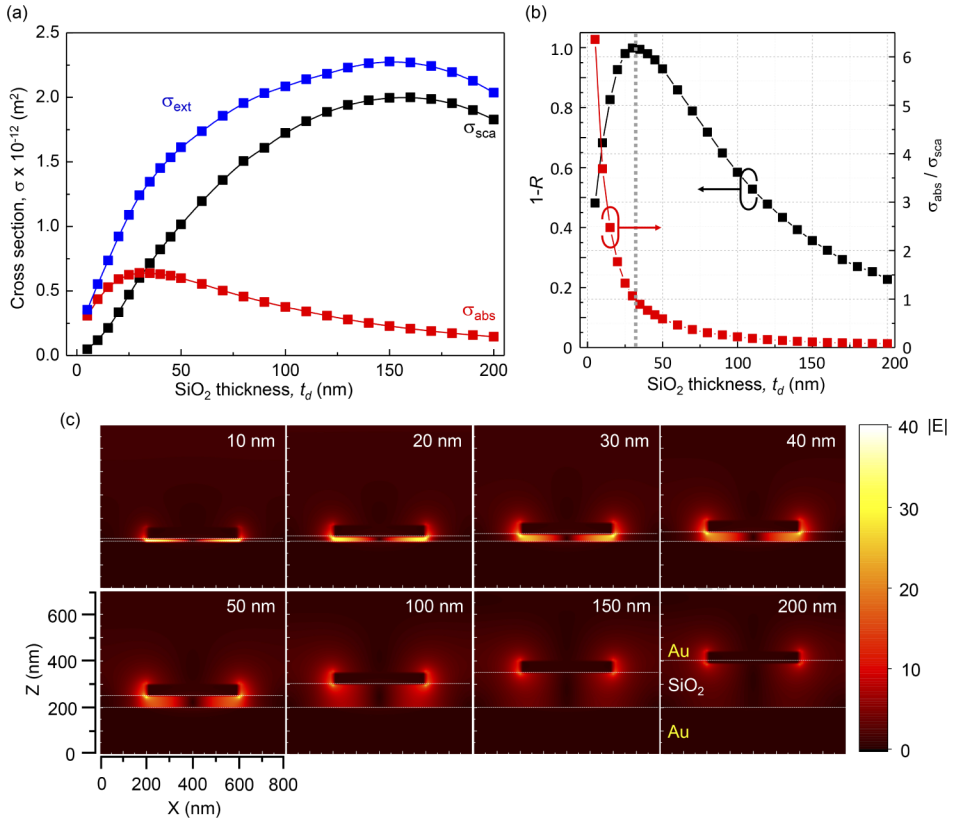


**Fig. 3.** (a) Plots of FDTD simulated cross-sections $\sigma_{abs}$, $\sigma_{sca}$, $\sigma_{ext}$ corresponding to metasurface minimum reflection spectral condition as a dependence on insulator layer thickness. (b) Dependence of the $\sigma_{abs}/\sigma_{sca}$ ratio and 1-$R$ on $SiO_2$ thickness. (c) FDTD simulated cross-sectional views of resonant electromagnetic field field intensity localization in MIM structures with different insulator layer thicknesses.

insulator layer is bound to eventually be converted to thermal energy in the free-carrier plasma of metals in the MIM structure. However, the portion loosely confined around a nanodisc particle is liable to re-radiated into free space, and should be considered as scattered. Hence, for our $D$ = 400 nm disc diameter metasurfaces, $t_d$ = 30 nm insulator thickness defines a delimiting line between the absorption dominated mode ($t_d \leq$ 30 nm) and primarily scattering mode for $t_d \geq$30 nm. According to the temporal coupled-mode theory, $\sigma_{abs}$ and $\sigma_{sca}$ are related to the non-radiative ($\gamma_i$) and radiative ($\gamma_e$) decay rates respectively. Equality between the two rates $\gamma_i = \gamma_e$ is essentially required for the critical coupling condition to be met [60].

This relationship between absorbance and scattering processes is distinctly observable for nanodisc type of metasurfaces, and is outlined in Fig. 4(a), which summarizes FDTD simulated reflectance and absorbance/scattering behavior as a function of a comprehensive MIM metasurface parameter study, including sweeps of $SiO_2$ thickness $t_d$ from 10 to 100 nm in 10 nm increments, disc diameter $D$ from 400 to 800 nm in 100 nm steps, and the ratio of $P/D$ from 1.5 to 3.0 in 0.5 steps. In both $R$ and $\eta = \sigma_{abs}/\sigma_{sca}$ plots, minimum reflectance (i.e. maximum extinction *Ext*) condition is observed along a relatively narrow parameter range band, corresponding to bright-yellow areas. This minimum reflectance condition closely matches the $\sigma_{abs}/\sigma_{sca} = 1$ dividing curve (white-band) between where the metasurface is primarily absorbing (red area) and mainly scattering (blue area). Overall, increasing the disc diameter relaxes the constraints on

Optics EXPRESS

$SiO_2$ thickness $t_d$, so that comparable localization can be achieved for larger insulator spacing. Furthermore, increasing nanodisk pattern periods tends to similarly increase the apparent contribution of absorbance, but this is likely due to a simple decrease in the number of dipolar scatterers per unit surface area.

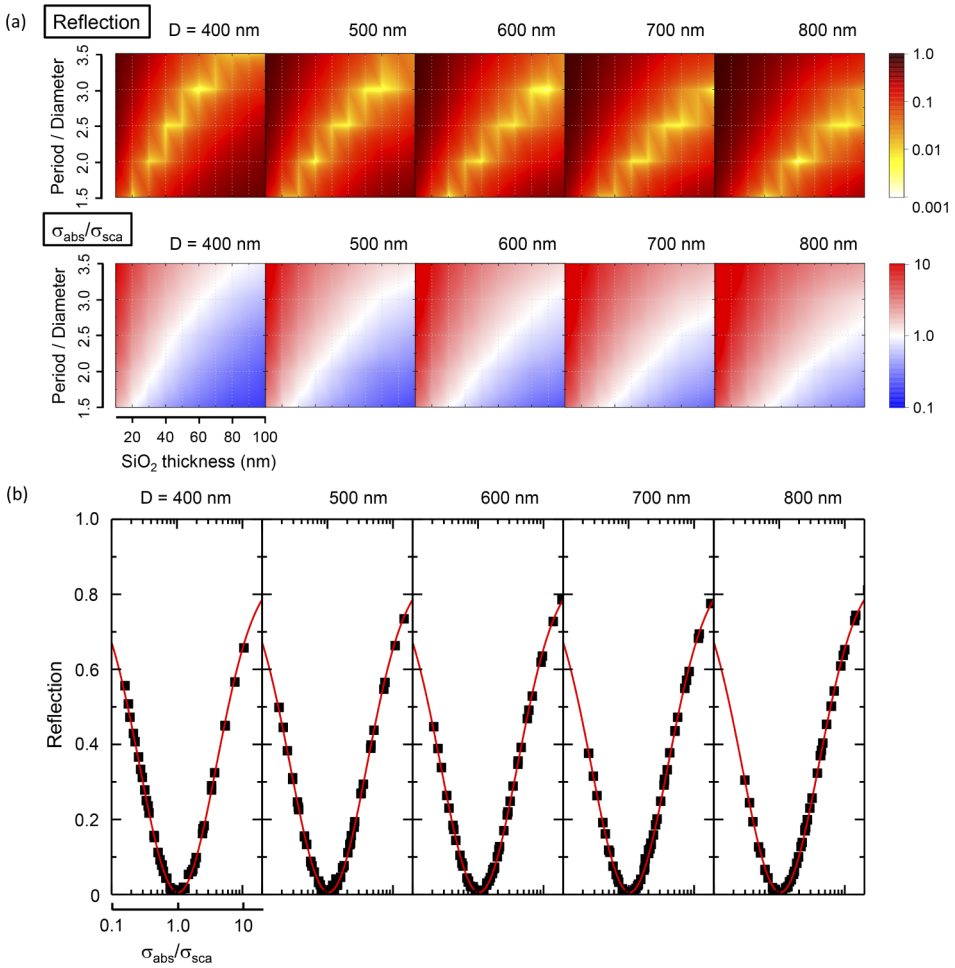


**Fig. 4.** FDTD simulated parameter sweeps of metasurface-radiation interaction behavior. (a) Comprehensive parameter study of reflectance (top) and absorption/scattering cross-section ratio (bottom) dependence on disc diameter $D$, period $P$ and $SiO_2$ thickness $t_d$. Grid line intersections correspond to simulated data points. (b) Relation between minimum reflectance and absorption/scattering cross section ratio, corresponding to respective disc diameter $D$ panels in (a). Different data points in plots for a given $D$ correspond minimum reflectance attained using each combination of $P/D$ and $t_d$ value pairs.

All minimum reflectance $R$ data points, extracted from spectra calculated for each combination of 5 $P/D$ and 10 $t_d$ parameters (50 data points in total), are plotted against $\sigma_{abs}/\sigma_{sca}$, as shown in Fig. 4(b). The resulting dependencies can be readily fitted by the same Gaussian curve. We concluded that in the simple system of low loss metal (Au) and dielectric ($SiO_2$) metasurfaces limits the achievable maximum of $\eta$ at the perfect anti-reflection $R \rightarrow 0$ condition.

Panels in Fig. 5 show $\sigma_{abs}/\sigma_{sca}$ relationships with $\sigma_{abs}$, $\sigma_{sca}$, and $\sigma_{ext}$, respectively, each normalized by the resonance wavelength. This graph reveals the maximum attainable absorbance,

Optics EXPRESS

scattering and total extinction cross-section for a selected efficiency $\eta$. All the plotted data points are clustered around the $\sigma_{abs}/\sigma_{sca} = 1$ condition. It is important to note that the maximum $\sigma_{abs}$ appears at $\sigma_{abs}/\sigma_{sca} \geq 1$, whereas the maximum $\sigma_{sca}$ appears at $\sigma_{abs}/\sigma_{sca} \leq 1$. Consequently, the maximum of $\sigma_{ext}$ is situated at $\sigma_{abs}/\sigma_{sca} = 1$. Estakhri et. al. reported that gold/$SiO_2$ core-shell structures always exhibit maximum $\pi\sigma_{abs}/\lambda^2$ at $\sigma_{abs}/\sigma_{sca} = 1$ as well [48]. Therefore, the observed tendency of $\sigma_{sca}$ to be tied to $\sigma_{abs}$ is expected and is defined by general plasmonic particle scattering dynamics.

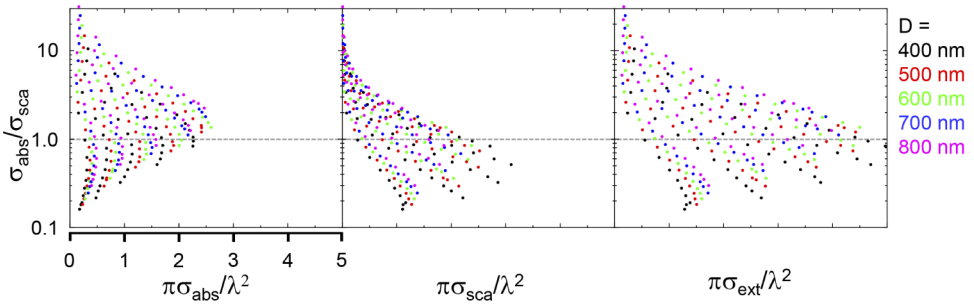


**Fig. 5.** Plots of $\sigma_{abs}/\sigma_{sca}$ in relation to the normalized cross-sections of absorption $\pi\sigma_{abs}/\lambda^2$, scattering $\pi\sigma_{sca}/\lambda^2$, and extinction $\pi\sigma_{ext}/\lambda^2$ for different metasurface disk diameters $D$.

While the extinction cross-section $\sigma_{ext}$ underlies the extinction $Ext = 1 - R$, it is nevertheless challenging to maximize the $\sigma_{abs}$ at the minimal reflectance. This is a severe impediment for the realization of true perfect absorption $A \rightarrow 1$, and, by extension, perfect thermal emitters with emittance $E = A$ as per Kirchhoff's law of thermal radiation. From the simulated far-field distribution of scattered radiation, even though specular reflection is dominant in the FDTD analysis of ideal structures, it can be recognised that there is appreciable output at angles up to 40 degrees from the normal incidence. Therefore it is required to separate the specular reflection from scattering for further qualitative analysis that would be predictive of metasurface behavior as observed in the far-field.

### 3.1. *Increasing $\sigma_{abs}$ using an absorption layer: model and experiment*

**Model.** One possible approach for increasing the total absorption cross-section involves increasing the absorbance of electromagnetic radiation in metasurface materials. The electromagnetic field localized inside the $SiO_2$ insulator layer decays primarily the ohmic loss of the metals in MIM structure. However, Cr metal, widely used as an adhesion layer for noble metal plasmonic structures, exhibits a 5 times higher resistance than that of Au. This higher ohmic loss is expected to increase the rate of optical damping, thereby limit the fraction of energy that is available to be re-radiated by way of scattering to free-space. On the other hand, increasing the conductivity of the insulator layer causes the plasmon resonance to disappear [16]. Therefore, it is important not to compromise insulation between the metal reflector layer and the nanodiscs comprising a MIM structure.

In a previous study we have shown that the addition of Cr notably increased the extinction $Ext = 1 - R$ of a metasurface even for layer thicknesses as low as 5 nm [14]. Therefore, it is expected that when the thickness of a Cr adhesion layer is increased further, the absorption cross-section also would be augmented. Figure 6 shows the results of FDTD simulations with different Cr layer thicknesses ranging between 0 nm and 50 nm. There was a clearly observable departure from the $\sigma_{abs}/\sigma_{sca} = 1$ condition, denoted by $\Delta$, as the amount of Cr was increased. Indeed, $\Delta$ increased from 1 when adhesion layer effects were disregarded, up to 1.25 when Cr layer thickness was 50 nm. These simulation results strongly suggest that the absorption/scattering

Optics EXPRESS

ratio can be adjusted by controlling the thickness of an absorption layer interspersed between insulator and Au on both sides of the MIM stack. Fig. 6(c) shows FDTD calculated optical reflection spectra from a periodic array of nanodisks with 50 nm Cr and without (W/O) Cr. The simulated MIM structure had disc diameter set as 1000 nm, periodicity 2000 nm, and $SiO_2$ thickness $t_d$ was 200 nm. In both spectra, the main resonance peak appeared at around 5.8 $\mu$m and close to zero minimum reflectance was realized. Furthermore, inclusion of a Cr layer was associated with a reduction of reflectance at shorter wavelengths from 0.5 to 4 $\mu$m, owing to absorption in Cr.

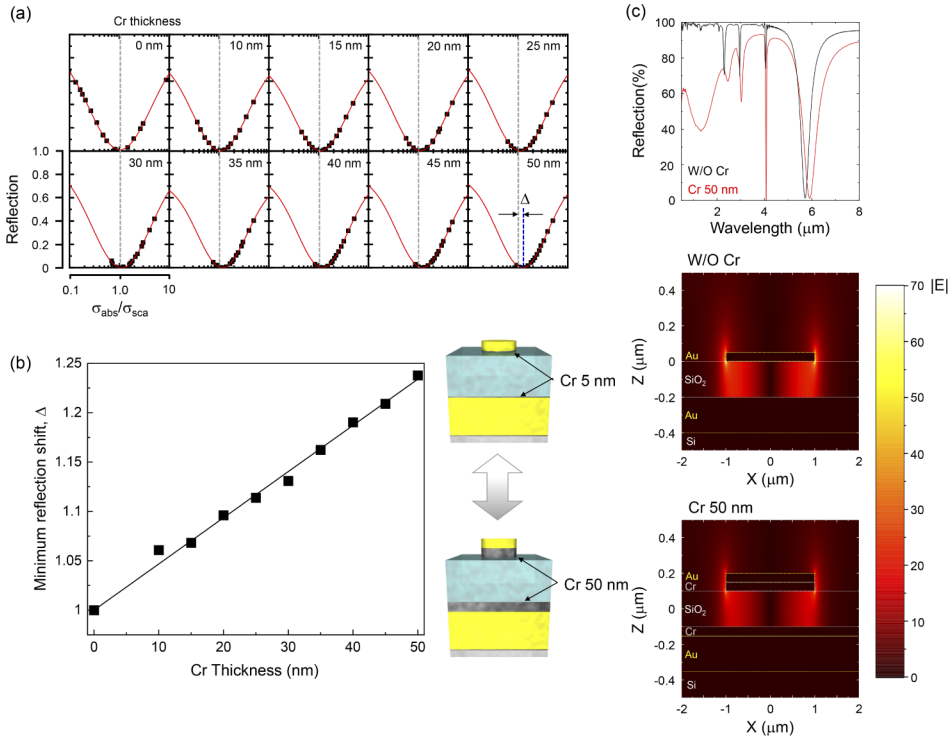


**Fig. 6.** (a) FDTD simulated relation between minimum reflectance and absorption/scattering cross-section ratio $\sigma_{abs}/\sigma_{sca}$, corresponding to different Cr adhesion layer thicknesses ranging from 0 nm to 50 nm. (b) Cr layer thickness dependence plot of Δ, which is the $\sigma_{abs}/\sigma_{sca}$ value at minimum reflectance. (c) Reflectance spectra and cross-sectional electromagnetic field distribution images comparing nanodisk performance without and with 50 nm thickness Cr layer. The Au disc diameter is 1000 nm, periodicity is 2000 nm, and $SiO_2$ insulator thickness $t_d$ is 200 nm.

In both structures, strongest electromagnetic field appeared at the interface between $SiO_2$ and metal nanostructures. Consequently, when Cr is present, optical field is confined in the vicinity of the absorbing Cr instead of Au. Stronger damping reduces $|E_{max}|/|E_0|$ from ~ 70 without Cr down to ~ 50 with Cr. Gold exhibits a low loss electron conductivity and therefore is able to generate strong scattering of electromagnetic energy localized in its vicinity. On the other hand, Cr, which is relatively lossy, rapidly absorbs optical energy and is only able to maintain a limited level of field localization. As mentioned previously, then plasmon resonance vanishes if the electric conductivity of insulator layer is increased. However, this MIM structure with Cr absorber layers ensures that the $SiO_2$ layer insulation between both metallic parts of the MIM structure is maintained.

Optics EXPRESS

**Experiment.** We experimentally tested the effect of Cr absorption layer inclusion in a metasurface. MIM samples were made with 5 nm and 50 nm Cr adhesion layer thicknesses, as illustrated in the inset of Fig. 6. In order to benchmark experimental finding against FDTD simulation results, other parameters of the fabricated samples were varied as well - thicknesses of $SiO_2$ insulator layers were 100, 150, 200 nm, disc diameters ranged from 600 to 4000 nm (with a 50 nm increment up to 2000 nm diameter, and 100 nm increment between 2000 nm and 4000 nm). The measured optical reflectance and thermal radiation emission spectra with selected data are shown in Figs. 7 and 8 for 5 nm and 50 nm Cr thickness cases, respectively. Also, the maximum radiation emittance at resonance wavelength was plotted against the minimum reflection using all available experimental data. The dashed "Kirchhoff's line" indicates the upper limitation of radiation output efficiency when reflection is directly tied to absorbance as $A = 1 - R$. As predicted by FDTD simulations, the $SiO_2$ thickness alters the Au disc diameter value at which a near-perfect absorption condition is achieved. For a $t_d$ = 100 nm $SiO_2$ thickness, the minimum reflection resonance was situated at $\lambda \sim 3.5$ $\mu$m; for 150 nm - $\lambda \sim 4.5$ $\mu$m; and for 200 nm - $\lambda \sim 6.5$ $\mu$m, respectively. For thinner 5 nm Cr layers, reflectance and radiation emission spectra closely mirror each other. However, the emittance was unable to exceed the 80% black body value, even when a metasurface exhibits near total reflectance suppression. This divergence between measured optical extinction and radiation emission is most apparent at higher wavelengths, likely due to lower optical absorbance of Au in that spectral region.

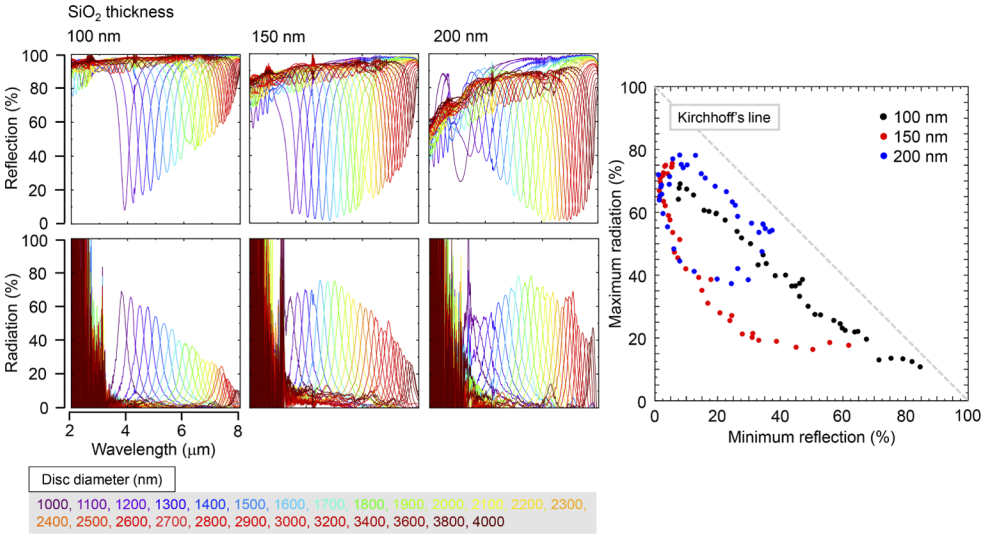


**Fig. 7.** Experimentally measured reflectance (top) and thermal radiation emittance (bottom) for a series of metasurfaces with a 5 nm Cr adhesion layer and 100, 150, 200 nm $SiO_2$ spacer thicknesses. Right panel plots maximum radiation emittance against the minimum reflection at resonance wavelength. The Kirchhoff's line represents the condition $A = 1 - R$.

When Cr thickness was increased to 50 nm to aid in absorbance, spectral behaviors changed drastically. The reflectance at shorter wavelengths was further suppressed due to absorption in Cr, although this also involved the reduction in metasurface quality factor and an increased resonance linewidth. Furthermore, the minimum anti-reflection parameter range became broader than that for a thinner Cr layer. In case of $SiO_2$ $t_d$ = 100 nm, reflectance became less than 10% throughout the 2-to-6 $\mu$m wavelength window. The thermal radiation output was also considerably improved compared to the MIM design using 5 nm Cr thickness, with maximum radiation exceeding 90% emittance. This illustrates that, due to absorption in the Cr layer, absorbance in MIM pattern became dominant relative to scattering. This can serve as a guideline for designing metasurfaces

Optics EXPRESS

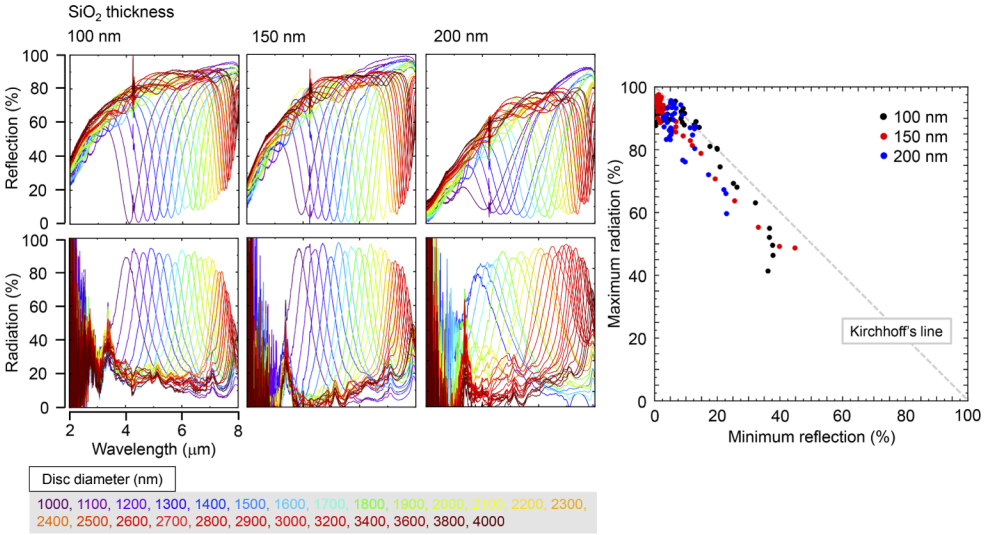


**Fig. 8.** Experimentally measured reflectance (top) and thermal radiation emittance (bottom) for a series of metasurfaces with a 50 nm Cr adhesion layer and 100, 150, 200 nm $SiO_2$ spacer thicknesses.Right panel is the plot of maximum radiation to the minimum reflection at resonance wavelength. The Kirchhoff's line is the condition of $A = 1 - R$.

that perform closer to the true perfect absorption condition $A \rightarrow 1$. As shown by FDTD simulated and experimental reflectance and radiation emission spectra, the addition of a Cr layer resulted in a broadening of resonance linewidths. These results indicate that a $\gamma_i \gg \gamma_e$ condition, in keeping with $\gamma_i + \gamma_e \ll \omega_0$, is realized when Cr is applied, whereas narrowband super scattering materials generally satisfy the opposite relationship $\gamma_e \gg \gamma_i$ [61,62]

Other possible metals for controlling MIM absorbance as alternatives to chromium, which, as previously mentioned, has a 5 times larger resistance than gold, are: Ti with 17 times larger resistance, Bi 45 times, and Mn 105 times. Titanium is also frequently used as an adhesion layer between Au and $SiO_2$, and it is usually considered that its detrimental effect on plasmonic properties of Au is smaller than Cr. Furthermore, not only the conductivity of a metal, but also its optical permittivity should be considered for the realization of true-perfect absorber, hence, a perfect thermal black-body emitter $A = E = 1$ (100%).

## 4. Conclusions and outlook

In this study, we have *quantitatively* analyzed the scattering effects by numerical modeling as well as fabrication and characterization of MIM metasurfaces. We observed the considerable effect backwards scattering has on the optical response of metasurfaces, hence it is a prominent feature that cannot be ignored in their design. Also, there is further room for improvement in removing the specular reflection of metasurfaces, guided by detailed FDTD analysis. Light scattering under slanted incidence is the next required step for analysis of MIM response and can be achieved at a *quantitative* level using FDTD modeling. We show that it is possible to increase the absorption cross section via use of nano-thin layers of metals with strong absorbance such as Cr. This point was confirmed experimentally by showing that a higher Cr adhesion layer thickness was able to drastically improve thermal radiation output efficiency from MIM metasurfaces. Thermal radiation due to a large enhancement of infrared absorption together with a strong coupling disk and base-plate in MIM metasurfaces [30,41] provides a promising

Optics EXPRESS

approach to realize a perfect absorber at the IR molecular fingerprinting spectral range with wide applicability in diverse sensing contexts.

**Funding.** Australian Respiratory Council (LP190100505); Japan Society for the Promotion of Science (19F19071, 20H02545, JPJSBP1); Adaptable and Seamless Technology Transfer Program through Target-Driven R and D (19216760).

**Disclosures.** The authors declare no conflicts of interest.

**Data availability.** Data underlying the results presented in this paper are not publicly available at this time but may be obtained from the authors upon reasonable request

## References

1. S. Lundgaard, S. H. Ng, Y. Nishijima, M. Mazilu, and S. Juodkazis, "Black metals: optical absorbers," Micromachines **11**(3), 256 (2020).
2. Y. Nishijima, H. Nishijima, and S. Juodkazis, "Black silicon as a highly efficient photo-thermal converter for snow/ice melting in early spring agriculture," Sol. Energy Mater. Sol. Cells **217**, 110706 (2020).
3. R. Komatsu, A. Balčytis, G. S. amd T. Yamamura, Y. Nishijima, and S. Juodkazis, "Plasmonic photo-thermoelectric energy converter with black-si absorber," Sol. Energy Mater. Sol. Cells **143**, 72–77 (2015).
4. S. H. Cho, M. Seo, J. H. Kang, J. K. Yang, S. Y. Kang, K. H. Hwang, B. D. Lee, J. G. Lee, Y. W. Song, J. H. Lee, and Y. H. Lee, "A black metal-dielectric thin film for high-contrast displays," J. Korean Phys. Soc. **55**(2), 501–507 (2009).
5. Z. Yu, A. Raman, and S. Fan, "Fundamental limit of nanophotonic light trapping in solar cells," Proc. Natl. Acad. Sci. U. S. A. **107**(41), 17491–17496 (2010).
6. N. I. Landy, S. Sajuyigbe, J. J. Mock, D. R. Smith, and W. J. Padilla, "Perfect metamaterial absorber," Phys. Rev. Lett. **100**(20), 207402 (2008).
7. S. Liu, H. Chen, and T. J. Cui, "A broadband terahertz absorber using multi-layer stacked bars," Appl. Phys. Lett. **106**(15), 151601 (2015).
8. R. Alaee, M. Farhat, C. Rockstuhl, and F. Lederer, "A perfect absorber made of a graphene micro-ribbon metamaterial," Opt. Express **20**(27), 28017–28024 (2012).
9. Y. Cui, J. Xu, K. H. Fung, Y. Jin, A. Kumar, S. He, and N. X. Fang, "A thin ?lm broadband absorber based on multi-sized nanoantennas," Appl. Phys. Lett. **99**(25), 253101 (2011).
10. J. Hendrickson, J. Guo, B. Zhang, W. Buchwald, and R. Soref, "A wide-band perfect light absorber at mid-wave infrared using multiplexed metal structures," Opt. Lett. **37**(3), 371–373 (2012).
11. Z. Yu, G. Veronis, and S. Fan, "Design of midinfrared photodetectors enhanced by surface plasmons on grating," Appl. Phys. Lett. **89**(15), 151116 (2006).
12. M. Pu, C. Hu, M. Wang, C. Huang, Z. Zhao, C. Wang, Q. Feng, and X. Luo, "Design principles for infrared wide-angle perfect absorber based on plasmonic structure," Opt. Express **19**(18), 17413–17420 (2011).
13. K. Chen, R. Adato, and H. Altug, "Dual-band perfect absorber for multispectral plasmon-enhanced infrared spectroscopy," ACS Nano **6**(9), 7998–8006 (2012).
14. N. To, S. Juodkazis, and Y. Nishijima, "Detailed experiment- theory comparison of mid-infrared metasurface perfect absorbers," Micromachines **11**(4), 409 (2020).
15. P. Yu, L. V. Besteiro, J. Wu, Y. Huang, Y. Wang, A. O. Govorov, and Z. Wang, "Metamaterial perfect absorber with unabated size-independent absorption," Opt. Express **26**(16), 20471–20480 (2018).
16. Y. Nishijima, A. Balčytis, S. Naganuma, G. Seniutinas, and S. Juodkazis, "Tailoring metal and insulator contributions in plasmonic perfect absorber metasurfaces," ACS Appl. Nano Mater. **1**(7), 3557–3564 (2018).
17. C. W. Cheng, M. N. Abbas, C. W. Chiu, K. T. Lai, M. H. Shih, and Y. C. Chang, "Wide-angle polarization independent infrared broadband absorbers based on metallic multi- sized disk arrays," Opt. Express **20**(9), 10376–10381 (2012).
18. P. Wu, Z. Chen, H. Jile, C. Zhang, D. Xu, and L. Lv, "An infrared perfect absorber based on metal-dielectric-metal multilayer ?lms with nanocircle holes arrays," Results Phys. **16**, 102952 (2020).
19. X. He, S. Yan, G. Lu, Q. Zhang, F. Wu, and J. Jiang, "An ultra-broadband polarization independent perfect absorber for the solar spectrum," RSC Adv. **5**(76), 61955–61959 (2015).
20. F. Ding, J. Dai, Y. Chen, J. Zhu, Y. Jin, and S. I. Bozhevolnyi, "Broadband near-infrared metamaterial absorbers utilizing highly lossy metals," Sci. Rep. **6**(1), 39445 (2016).
21. C. Liang, Z. Yi, X. Chen, Y. Tang, Y. Yi, Z. Zhou, X. Wu, Z. Huang, Y. Yi, and G. Zhang, "Dual-band infrared perfect absorber based on a ag-dielectric-ag multilayer films with nanoring grooves arrays," Plasmonics **15**(1), 93–100 (2020).
22. U. Huebner, E. P. Severin, R. Alaee, C. Menzel, M. Ziegler, C. Rockstuhl, F. Lederer, T. Pertsch, H. G. Meyer, and J. Popp, "Exploiting extreme coupling to realize a metamaterial perfect absorber," Microelectron. Eng. **111**, 110–113 (2013).
23. C. Wu, B. Neuner, and G. Shvets, "Large-area wide-angle spectrally selective plasmonic absorber," Phys. Rev. B **84**(7), 075102 (2011).
24. B. Zhang, Y. Zhao, Q. Hao, B. Kiraly, I. C. Khoo, S. Chen, and T. J. Huang, "Polarization-independent dual-band infrared perfect absorber based on a metal-dielectric-metal elliptical nanodisk array," Opt. Express **19**(16), 15221–15228 (2011).

Optics EXPRESS


25. K. Aydin, V. E. Ferry, R. M. Briggs, and H. A. Atwater, "Broadband polarization-independent resonant light absorption using ultrathin plasmonic super absorbers," Nat. Commun. **2**(1), 517 (2011).
26. M. K. Hedayati, M. Javaherirahim, B. Mozooni, R. Abdelaziz, A. Tavassolizadeh, V. S. K. Chakravadhanula, V. Zaporojtchenko, T. Strunkus, F. Faupel, and M. Elbahri, "Design of a perfect black absorber at visible frequencies using plasmonic metamaterials," Adv. Mater. **23**(45), 5410–5414 (2011).
27. R. A. Pala, J. White, E. Barnard, J. Liu, and M. L. Brongersma, "Design of plasmonic thin-film solar cells with broadband absorption enhancements," Adv. Mater. **21**(34), 3504–3509 (2009).
28. L. Lei, S. Li, H. Huang, K. Tao, and P. Xu, "Ultrabroadband absorber from visible to near-infrared using plasmonic metamaterial," Opt. Express **26**(5), 5686–5693 (2018).
29. T. Kondo, S. Hasegawa, T. Yanagishita, N. Kimura, T. Toyonaga, and H. Masuda, "Control of thermal radiation in metal hole array structures formed by anisotropic anodic etching of Al," Opt. Express **26**(21), 27865 (2018).
30. M. Ryu, Y. Nishijima, S. Morimoto, N. To, T. Hashizume, R. Matsubara, A. Kubono, J. Hu, S. H. Ng, S. Juodkazis, and J. Morikawa, "Hyperspectral molecular orientation mapping in metamaterials," Appl. Sci. **11**(4), 1544 (2021).
31. M. Diem, T. Koschny, and C. M. Soukoulis, "Wide-angle perfect absorber/thermal emitter in the terahertz regime," Phys. Rev. B **79**(3), 033101 (2009).
32. H. T. Miyazaki, T. Kasaya, M. Iwanaga, B. Choi, Y. Sugimoto, and K. Sakoda, "Dual-band infrared metasurface thermal emitter for $co_2$ sensing," Appl. Phys. Lett. **105**(12), 121107 (2014).
33. M. W. Tsai, T. H. Chuang, C. Y. Meng, Y. T. Chang, and S. C. Lee, "High performance midinfrared narrow-band plasmonic thermal emitter," Appl. Phys. Lett. **89**(17), 173116 (2006).
34. Y. Nishijima, A. Balčytis, S. Naganuma, G. Seniutinas, and S. Juodkazis, "Kirchhoff's metasurfaces towards efficient photo-thermal energy conversion," Sci. Rep. **9**(1), 8284 (2019).
35. A. Lochbaum, Y. Fedoryshyn, A. Dorodnyy, U. Koch, C. Hafner, and J. Leuthold, "On-chip narrowband thermal emitter for mid-ir optical gas sensing," ACS Photonics **4**(6), 1371–1380 (2017).
36. N. Liu, M. Mesch, T. Weiss, M. Hentschel, and H. Giessen, "Infrared perfect absorber and its application as plasmonic sensor," Nano Lett. **10**(7), 2342–2348 (2010).
37. Z. Yong, S. Zhang, C. Gong, and S. He, "Narrow band perfect absorber for maximum localized magnetic and electric ?eld enhancement and sensing applications," Sci. Rep. **6**(1), 24063 (2016).
38. S. Luo, J. Zhao, D. Zuo, and X. Wang, "Perfect narrow band absorber for sensing applications," Opt. Express **24**(9), 9288–9294 (2016).
39. T. Beni, N. Yamasaku, T. Kurotsu, N. To, S. Okazaki, T. Arakawa, A. Balčytis, G. Seniutinas, S. Juodkazis, and Y. Nishijima, "Metamaterial for hydrogen sensing," ACS Sens. **4**(9), 2389–2394 (2019).
40. T. Kumagai, N. To, A. Balčytis, G. Seniutinas, S. Juodkazis, and Y. Nishijima, "Kirchhoff's thermal radiation from lithography-free black metals," Micromachines **11**(9), 824 (2020).
41. Y. Nishijima, S. Morimoto, A. Balčytis, T. Hashizume, R. Matsubara, A. Kubono, N. To, R. Meguya, J. Morikawa, and S. Juodkazis, "Coupling of molecular vibration and metasurface modes for efficient mid-infrared emission," J. Mater. Chem. C **10**(2), 451–462 (2022).
42. S. Feng and K. Halterman, "Coherent perfect absorption in epsilon-near-zero metamaterials," Phys. Rev. B **86**(16), 165103 (2012).
43. J. Yoon, M. Zhou, M. A. Badsha, T. Y. Kim, Y. C. Jun, and C. K. Hwangbo, "Broadband epsilon-near-zero perfect absorption in the near-infrared," Sci. Rep. **5**(1), 12788 (2015).
44. J. R. Hendrickson, S. Vangala, C. Dass, R. Gibson, J. Goldsmith, K. Leedy, D. E. Walker, J. W. Cleary, W. Kim, and J. Guo, "Coupling of epsilon-near-zero mode to gap plasmon mode for flat-top wideband perfect light absorption," ACS Photonics **5**(3), 776–781 (2018).
45. J. Kuttruff, D. Garoli, J. Allerbeck, R. Krahne, A. D. Luca, D. Brida, V. Caligiuri, and N. Maccaferri, "Ultrafast all-optical switching enabled by epsilon-near-zero-tailored absorption in metal-insulator nanocavities," Commun. Phys. **3**(1), 114 (2020).
46. P. N. Dyachenko, S. Molesky, A. Y. Petrov, M. Stormer, T. Krekeler, S. Lang, M. Ritter, Z. Jacob, and M. Eich, "Controlling thermal emission with refractory epsilon-near-zero metamaterials via topological transitions," Nat. Commun. **7**(1), 11809 (2016).
47. H. Hu, C. Ma, and Z. Liu, "Plasmonic dark ?eld microscopy," Appl. Phys. Lett. **96**(11), 113107 (2010).
48. N. M. Estakhri and A. Alu, "Minimum-scattering superabsorbers," Phys. Rev. B **89**(12), 121416 (2014).
49. C. Langhammer, Z. Yuan, I. Zoric, and B. Kasemo, "Plasmonic properties of supported pt and pd nanostructures," Nano Lett. **6**(4), 833–838 (2006).
50. C. Langhammer, B. Kasemo, and I. Zoric, "Absorption and scattering of light by pt, pd, ag, and au nanodisks: Absolute cross sections and branching ratios," J. Chem. Phys. **126**(19), 194702 (2007).
51. C. Langhammer, M. Schwind, B. Kasemo, and I. Zoric, "Localized surface plasmon resonances in aluminum nanodisks," Nano Lett. **8**(5), 1461–1471 (2008).
52. C. Langhammer, M. Schwind, B. Kasemo, and I. Zoric, "Gold, platinum, and aluminum nanodisk plasmons: material independence, subradiance, and damping mechanisms," ACS Nano **5**(4), 2535–2546 (2011).
53. D. R. Smith, S. Schultz, P. Markos, and C. M. Soukoulis, "Determination of e?ective permittivity and permeability of metamaterials from re?ection and transmission coe?cients," Phys. Rev. B **65**(19), 195104 (2002).
54. N. Maccaferri, Y. Zhao, T. Isoniemi, M. Iarossi, A. Parracino, G. Strangi, and F. D. Angelis, "Hyperbolic meta-antennas enable full control of scattering and absorption of light," Nano Lett. **19**(3), 1851–1859 (2019).

Optics EXPRESS

55. D. W. Lynch and W. R. Hunter, "Gold (Au)," in *Handbook of optical constants of solids I*, E. D. Palik, ed. (Academic, 1985).
56. D. F. Edwards, "Silicon (Si)," in *Handbook of optical constants of solids I*, E. D. Palik, ed. (Academic, 1985).
57. H. R. Philipp, "Silicon Dioxise ($SiO_2$) (Glass)," in *Handbook of optical constants of solids I*, E. D. Palik, ed. (Academic, 1985).
58. D. W. Lynch and W. R. Hunter, "Chromium (Cr)," in *Handbook of optical constants of solids II*, E. D. Palik, ed. (Academic, 1991).
59. Y. Nishijima, L. Rosa, and S. Juodkazis, "Surface plasmon resonances in periodic and random patterns of gold nano-disks for broadband light harvesting," Opt. Express **20**(10), 11466–11477 (2012).
60. Z. Ruan and S. Fan, "Temporal coupled-mode theory for light scattering by an arbitrarily shaped object supporting a single resonance," Phys. Rev. A **85**(4), 043828 (2012).
61. Z. Ruan and S. Fan, "Superscattering of light from subwavelength nanostructures," Phys. Rev. Lett. **105**(1), 013901 (2010).
62. Z. Ruan and S. Fan, "Design of subwavelength superscattering nanospheres," Appl. Phys. Lett. **98**(4), 043101 (2011).